



Original Article

Magnetic, DC Electrical, and Impedance Properties of Zn Doped Yttrium Iron Garnet Nanoparticles

Dao Thi Thuy Nguyet*, Nguyen Phuc Duong, Luong Ngoc Anh

*International Training Institute for Material Science (ITIMS), Hanoi University of Science and Technology,
1 Dai Co Viet, Hai Ba Trung, Hanoi, Vietnam*

Received 24 October 2022

Revised 07 February 2023; Accepted 07 February 2023

Abstract: $Y_3Fe_{5-x}Zn_xO_{12}$ with $x = 0; 0.02; 0.04; 0.06; 0.08; 0.1$ (YIG) particle materials were fabricated by sol-gel method combined with heat treatment at 900 °C and 1,000 °C with different annealing times (2 h and 5 h) and heating rates (5 °C/min and 2 °C/min). X-ray diffraction patterns show that the obtained samples are single crystalline phases at the condition of an annealing temperature of 900 °C for 5 h and a heating rate of 2 degrees/min. FESEM images of the samples show particle sizes from the submicron to the micrometer. The magnetization of the samples decreases as the doping concentration increases. I-V characteristics and complex impedance spectra at room temperature of samples were measured. The results show that the resistivity value of the doped samples decreases in the range of 5-6 orders in magnitude compared with that of the pure YIG sample. The contribution of the grain boundaries to the impedance was analyzed. The conducting process is explained due to the tunneling of charge carriers across the grain boundary.

Keywords: Yttrium iron garnet, Zn doping, magnetic properties, I-V characteristics, complex impedance spectra.

1. Introduction

Yttrium iron garnet $Y_3Fe_5O_{12}$ (YIG) belongs to the garnet family and has a cubic structure. Each unit cell contains eight chemical formulas of $\{Y_3\}[Fe_2](Fe_3)O_{12}$. The brackets show three different sublattices. In the cell, 24 Y^{3+} ions occupy the dodecahedral sites (made up of 8 O^{2-} ions), 16 Fe^{3+} ions occupy the octahedral sites (made up of 6 O^{2-} ions), and 24 other Fe^{3+} ions reside in the tetrahedral sites (made up of 4 O^{2-} ions). Owing to their high melting point, high resistivity at room temperature

* Corresponding author.

E-mail address: nguyet.daothithuy@hust.edu.vn

<https://doi.org/10.25073/2588-1124/vnumap.4786>

($10^{12} \Omega\text{cm}$), low electromagnetic loss, and high thermal stability, YIGs are often used in applications at high frequencies [1]. Recently, YIG has been the subject of sensing applications [2-8], especially those in the form of granules and thin films. Since the 1980 s, D'Amico et al., [9-11] have shown that the presence of covalently unbalanced doped ions such as Ca^{2+} , V^{5+} , Sn^{4+} , Zn^{2+} , etc. in the positions of Y^{3+} , Fe^{3+} ions of YIG causes resistance reduction because these ions act as impurities, creating charge carriers in the YIG crystal lattice. The conduction process was explained by the "hopping" mechanism of charge carriers [12], in which the conductivity of materials depends on their concentration and mobility [13]. These studies open application abilities for YIG in the field of sensors. In addition, YIG materials absorb radiation at infrared frequencies. Hence, they are convenient for applications such as infrared-sensitive sensors in which the device structure does not need an additional layer of photosensitive material as in other types of sensors using conventional semiconducting materials [10].

Doping ions with valences different from 3^+ in one of the three sublattices of YIG depends very much on their radius. Fe^{3+} ions in sublattice (d) have radius $r_{\text{Fe}^{3+}}(d) = 0.49 \text{ \AA}$ but Fe^{3+} ions in sublattice (a) have radius $r_{\text{Fe}^{3+}}(a) = 0.645 \text{ \AA}$ [1]. The fact is that V^{5+} ions with radius $r_{\text{V}^{5+}} = 0.335$ are suitable for the position in (d) sublattice [1] while In^{3+} ions with $r_{\text{In}^{3+}} = 0.79$ or Sn^{4+} ions with $r_{\text{Sn}^{4+}} = 0.69$ are suitable in (a) sublattice [1, 14]. Zn^{2+} ions ($r_{\text{Zn}^{2+}} = 0.745 \text{ \AA}$) are said to be suitable for the position in the octahedral sublattice of YIG particles as in Garcia's study [15, 16].

With the aim of increasing the carrier concentration in YIG material, in this work, doping Zn^{2+} ions with concentrations $x \leq 0.1$ into the crystal positions of Fe^{3+} was implemented. The Zn^{2+} doped YIG samples with chemical formula $\text{Y}_3\text{Fe}_{5-x}\text{Zn}_x\text{O}_{12}$ ($x = 0; 0.02; 0.04; 0.06; 0.08; 0.1$) were prepared by sol-gel method in which the technological conditions were changed to obtain single-phase samples at all doping concentrations. The sol-gel technology is a good choice for the fabrication of doped YIG film and granular samples because it allows the mixing of element components with low concentrations at the atomic scale and with low heat-treatment temperatures [17]. Based on the fabricated samples, the dependence of physical properties, namely crystal structure, magnetization, DC resistance, and complex impedance spectrum on the doping concentration was investigated and evaluated.

2. Experimental

The initial chemicals of $\text{Fe}(\text{NO}_3)_3$, Y_2O_3 , and $\text{Zn}(\text{NO}_3)_2$ with purities above 99% were used. In the first step, solid powder Y_2O_3 was dissolved in a 2M HNO_3 solution. Solutions of nitrate salts of metals were mixed according to the molar ratio of metal ions $[\text{Y}]:[\text{Fe}]:[\text{Zn}] = 3:(5-x):x$ and stirred continuously at room temperature. Secondly, a 3M citric acid solution was added to the above mixture in a molar ratio equal to three times the total moles of metal ions. The mixture was continuously stirred and gradually heated up to $80 \text{ }^\circ\text{C}$. The gel formation took place in 3 hours. The gel was then dried at $150 \text{ }^\circ\text{C}$ for 24 h and preheated at $350 \text{ }^\circ\text{C}$ for 2 h in the air. The fine powder remained after burning the gel was ground in an agate mortar and calcined at 900 and $1,000 \text{ }^\circ\text{C}$ for 2 h and 5 h. In the calcination process, two heating rates of $5 \text{ }^\circ\text{C}/\text{min}$ and $2 \text{ }^\circ\text{C}/\text{min}$ were used to investigate the crystallization.

The powder samples were checked by X-ray diffraction measurements on the Bruker system (Cu-K α , D2 Phaser) at room temperature, with scanning angles 2θ of $10\text{--}80$ degrees. The results were calibrated and analyzed using Fullprof software. The morphology of the particle samples was studied by a FESEM field-emission scanning electron microscope (JEOL JSM-7600 F). Energy dispersive X-ray (EDX) spectroscopy is used to evaluate the elemental composition of the particle samples.

The magnetization of the sample at room temperature was measured on a vibrating sample magnetometer (DMS) with applied magnetic fields up to 10 kOe.

The powder samples were pressed with a pressure of 20 MPa into pellets with a diameter of ~10 mm and thickness of ~1 mm for resistance measurements. These pellets were heat treated in an Ar/H₂ gas atmosphere (ratio 85:15) at 600 °C for 2 h and then were polished for *I* – *V* measurements using a four-probe technique. Total impedance spectroscopy (CIS) measurements at room temperature of these pressed samples were performed in the frequency (*f*) range from 1–100 kHz using the Hioki LCR 3522 Hitester measurement system. Colloidal silver is used as conductive electrodes. In the measurements, a voltage of 1 V was applied. The CIS data were analyzed using MEISP 3.0 software.

3. Results and Discussions

3.1. Structure and Morphology

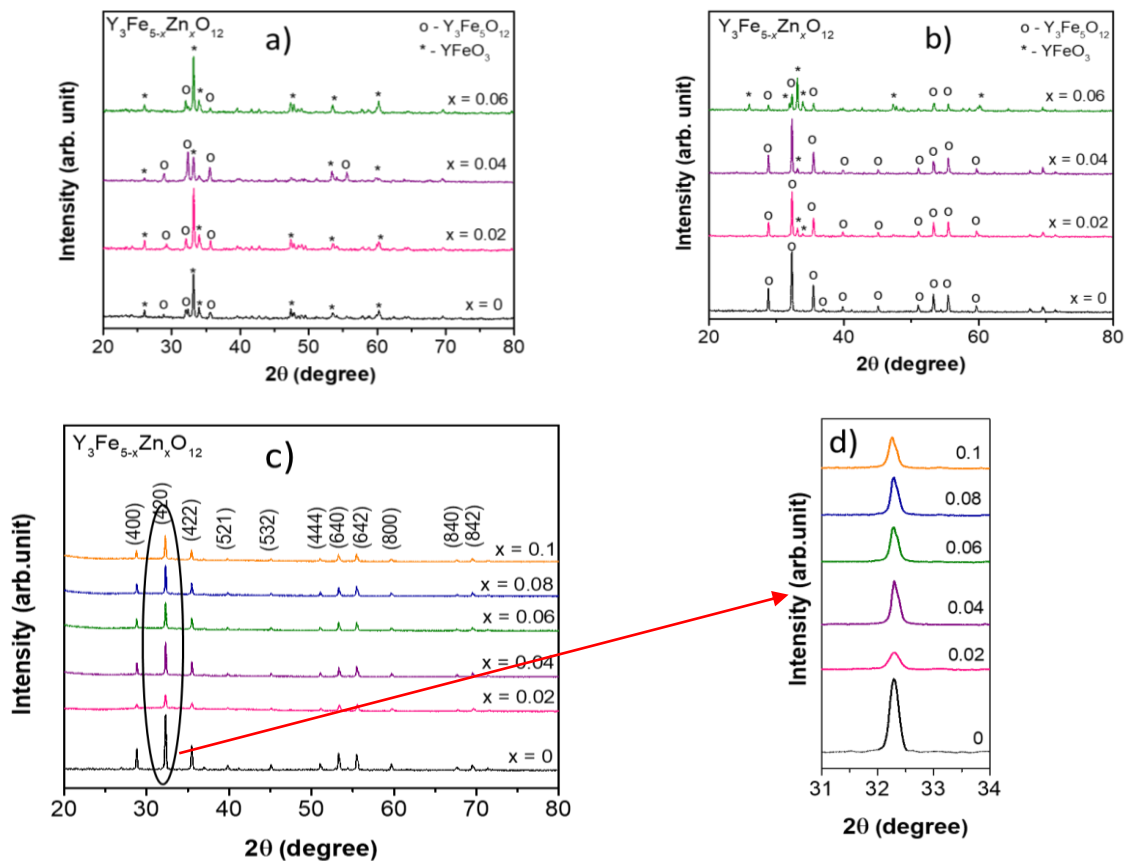


Figure 1. X-ray diffraction pattern of the Y₃Fe_{5-x}Zn_xO₁₂ samples denoted as series A (a), B (b) and C (c) and Magnified image of the diffraction peak (420) of series C (d).

The Y₃Fe_{5-x}Zn_xO₁₂ samples calcined at 900 °C for 2 h with a heating rate of 5 °C/min, at 1000 °C for 5 h with a heating rate of 5 °C/min, at 900 °C for 5 hours with a heating rate of 2 °C/min were prepared and denoted as A, B, and C series, respectively. Their X-ray diffraction patterns are shown in Figs. 1a, 1b, and 1c. The results show that the A and B series with a heating rate of 5 °C/min are not of a single phase. Besides the main garnet structure, a tiny amount of YFeO₃ exists. Single-phase samples

formed after annealing at 900 °C for 5 h with a heating rate of 2 °C/min (Fig. 1c). Fig. 1d is a magnified image of the diffraction peak (420) of the samples in Fig. 1c, which shows a shift of the diffraction peak towards smaller 2θ as the Zn content increases, corresponding to an increase of the lattice constant.

The lattice constants of the sample system were calculated using Fullprof software and are shown in Table 1, which increases as the doped Zn content increases. This phenomenon is due to the fact that Zn^{2+} ions participated in the structure of YIG and with an ionic radius larger than that of Fe^{3+} ion, they cause an expansion of the crystal lattice. The lattice constant of the YIG sample (C) is consistent with the value of the bulk sample, namely 12.376 Å, according to Gilleo's research [1]. The average crystal sizes determined by Sherrer' formula from the X-ray diffraction patterns of the samples ranged from 35 to 52 nm, as shown in Table 1. Comparison of the X-ray diffraction results at three heat treatment conditions as in Fig. 1a, b, and c, increasing the annealing temperature and annealing time (from 900 °C for 2 h to 1.000 °C for 5 h) reduces the amount of secondary phase formed (Fig. 1a and b) but for the doped samples, the slower heating rate results in better diffusion of the doped ions into the crystal of YIG (Fig. 1c).

The size and morphology of the $\text{Y}_3\text{Fe}_{5-x}\text{Zn}_x\text{O}_{12}$ ($x = 0; 0.06; 0.1$) particles were investigated via FESEM images (Fig. 2). The sizes of the particles in the series C are in the range of 200 nm – 1 μm (Fig. 2a) while for the series B the majority of the particles have the sizes in the scale of few millimeters (Fig. 2b). The results show that the size of the particles increases significantly at the higher annealing temperature. Samples of different chemical compositions under the same heat treatment conditions showed no difference in particle size. Therefore, one can conclude that with a small doping content, there is no significant effect on the particle size of the samples.

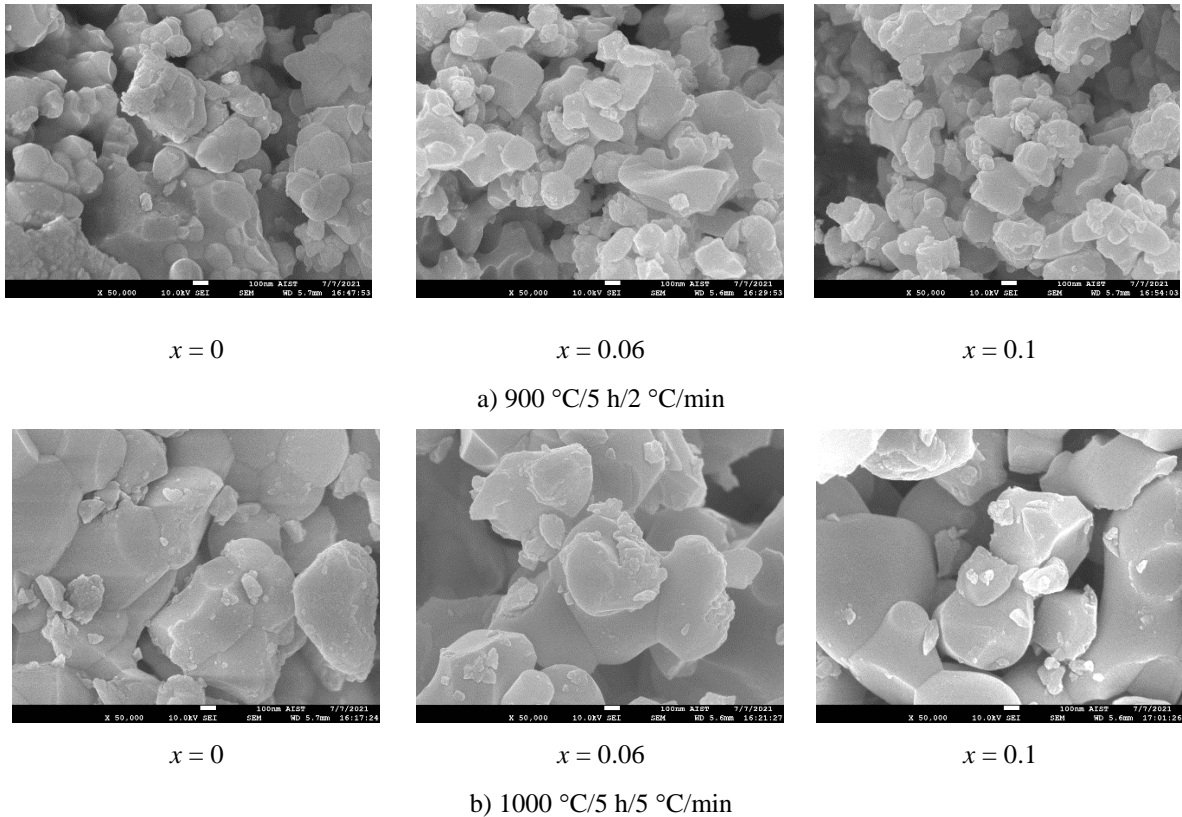


Figure 2. FESEM images of samples $Y_3Fe_{5-x}Zn_xO_{12}$ of series C (a) and series B (b).
The scale bar on the image corresponds to 100 nm length.

X-ray energy scattering spectra of the samples shown in Fig. 3 indicate the presence of Y and Fe elements in the two samples $x = 0$ (Figs. 3a, 3d) and the presence of element Zn in the doped samples $x = 0.06$ and 0.1 (Figs. 3b, 3c, 3e, 3f).

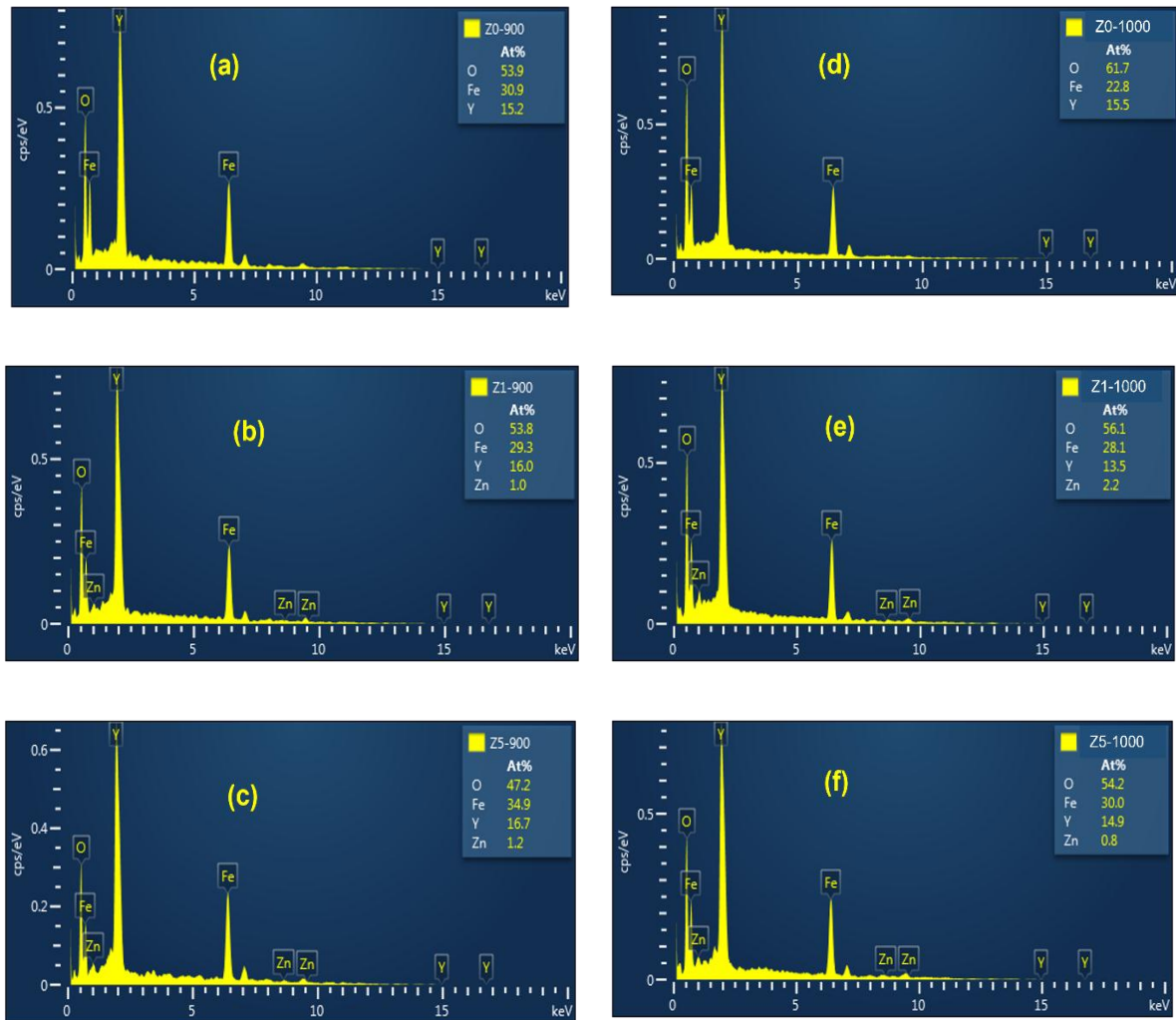


Figure 3. X-ray energy scattering spectra of $Y_3Fe_{5-x}Zn_xO_{12}$ samples: Series C: $x = 0$ (a); $x = 0.06$ (b); $x = 0.1$ (c) and series Figure 3. X-ray energy scattering spectra of $Y_3Fe_{5-x}Zn_xO_{12}$ samples: Series C: $x = 0$ (a); $x = 0.06$ (b); $x = 0.1$ (c) and series B: $x = 0$ (d); $x = 0.06$ (e); $x = 0.1$ (f).

3.2. Magnetization Process

The $M-H$ magnetization curves at room temperature of the single-phase (C) of $Y_3Fe_{5-x}Zn_xO_{12}$ samples are shown in Fig. 4. The results illustrate that the magnetization of the samples approaches saturation when increasing the applied magnetic field above $H \sim 2500$ Oe. The magnetization is almost

constant between 2,500 Oe and the maximum applied magnetic field of 9,600 Oe. The values of the technical saturation M_s of the samples were determined by linearly extrapolating the part of the magnetization curve in the high magnetic region to the magnetic field $H = 0$ and are listed in Table 1. The saturation magnetizations of our samples are larger compared to that of the particle samples fabricated by the same method by Garcia [15, 16], and Guo [18]. This result shows that our samples have larger crystallinity. The M_s values decrease gradually with the doping x concentration, indicating that Zn^{2+} ions have participated in the sublattice in the YIG crystals. The decrease of M_s value with x is consistent with the model on the location of the Zn^{2+} ion in octahedral sublattice as discussed in previous studies [3, 9, 15, 16]. Based on this model, the total magnetic moment of the ferrimagnetic structure is calculated according to the formula $m^{tot} = m^{Fe} \times (3-x) - m^{Fe} \times 2$, where the first term is the magnetic moment of the tetrahedral sublattice, and the second term is the magnetic moment of the octahedral sublattice; m^{Fe} is the magnetic moment of the Fe^{3+} ion ($5 \mu_B$). Since Zn^{2+} is a non-magnetic ion, as the doping concentration x increases, the magnetic moment of the octahedral sub-lattice decreases, and hence the saturation magnetism.

3.3. DC Characteristic

The I – V characteristics of the single-phase series C were investigated in the voltage range of ± 5 V at room temperature. For the pure sample ($x = 0$), the electric current cannot be detected due to a very large resistance of the samples. For the doped samples, linear I – V behavior is observed (Fig. 5), indicating the ohmic conduction in the applied voltage range. The experiments show that the resistance of the doped samples is reduced compared to that of the pure sample. At an applied voltage of 1 V, the DC resistivity of the samples is calculated by following formula:

$$\rho = \frac{RA}{L} \quad (1)$$

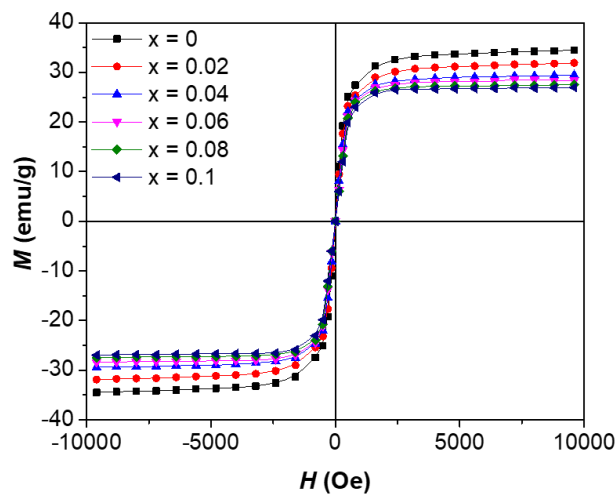


Figure 4. Hysteresis curves of series C at room temperature.

where R is the resistance, $A = \pi r^2$ is the area and L is the thickness of the pressed sample.

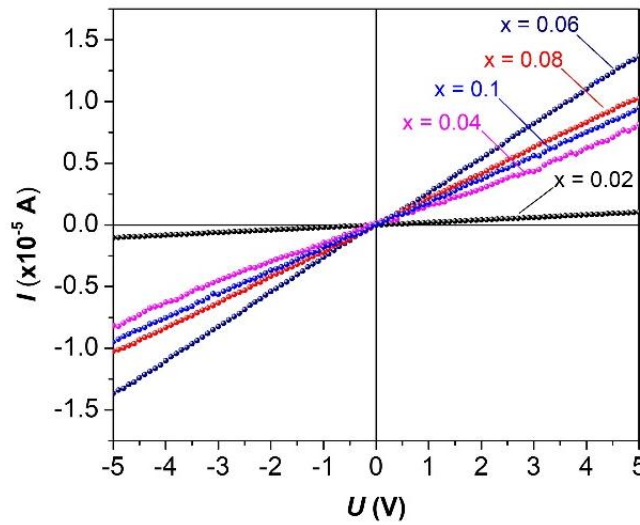


Figure 5. I - V characteristic of series C at room temperature.

The resistivity values of the samples are shown in Table 1. The results show that the resistivity value of the doped samples is 5–6 orders in magnitude smaller than that of the pure YIG sample prepared by the solid phase reaction method, according to previous studies (about $10^{12} \Omega\text{cm}$) [9]. The resistivity decreases sharply with increasing doping content to $x = 0.06$. At higher doping concentrations, resistivity does not change much. This result confirms that the presence of Zn^{2+} ions in the Fe^{3+} sublattice caused a charge imbalance at the region surrounding the Zn^{2+} ions. The generated charges shift across the samples under the applied electric field. The decrease in the resistivity value was also observed in other doped spinel and YIG samples [20, 21]. The small change in the resistivity value at higher doping concentrations x above 0.06 may be due to the uneven distribution of Zn^{2+} in the lattice cells. In addition, resistivity depends on other factors such as porosity and grain boundary contribution. Studies by Montes, Alaa, Guziewicz, and Li [22-25] have shown the relationship between the sample porosity, the influence of grain boundaries, and the electrical resistance of pressed powder metal samples as well as sintered oxide compounds.

Table 1. The lattice constant, crystal size, grain size, saturation magnetic, and DC resistivity at room temperature of series C

Samples	$x = 0$	$x = 0.02$	$x = 0.04$	$x = 0.06$	$x = 0.08$	$x = 0.1$
a (Å)	12.381	12.383	12.386	12.39	12.392	12.399
D_{XRD} (nm)	37	38	37	38	39	37
D_{FESEM} (nm)	120-150	120-150	120-150	120-150	120-150	120-150
$M_s^{300\text{K}}$ (emu/g)	32.7	30.31	28.3	28.19	27.4	26.4
ρ (10^6 Ohm. cm)	-	16	2	0.46	0.47	0.48

3.4. Complex Impedance Spectra

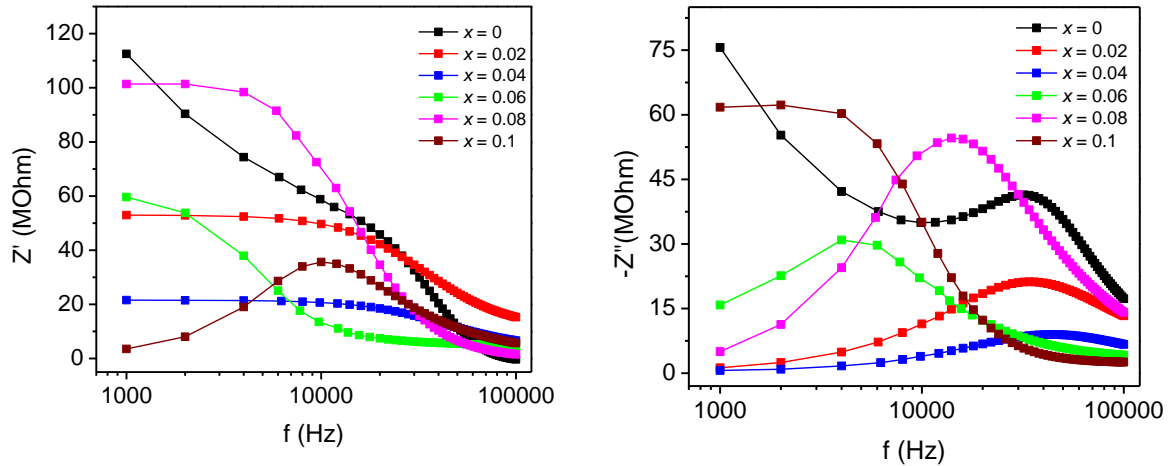


Figure 6. Frequency dependence of the real Z' (a) and imaginary Z'' (b) components of the complex impedance of series C.

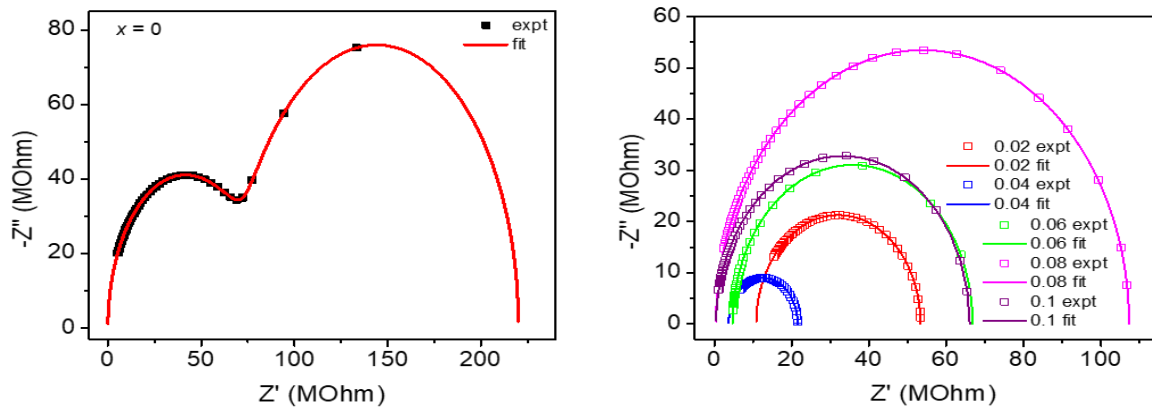


Figure 7. Nyquist plots of series C at room temperature. The solid lines are the fitting lines according to the simulated circuit diagram in Figure 8.

To better understand the contribution of grain boundaries, we investigated the complex impedance spectrum of single-phase samples at room temperature in the frequency range of 1 – 100 kHz (due to the limit of measuring equipment). As indicated in Section 3.1, the fabricated samples are a collection of randomly arranged particles. The grain boundary region contains deformed chemical bonds due to the relative misalignment of the crystal faces in adjacent grains resulting in different grain boundary properties from those of the material within the grains. The flow of charge transfer between two conductive electrodes depends on the properties of the particle, the grain boundary, and the electrode itself. Thus, such an electronic assembly can be thought of as a particle-particle boundary-electrode system, in which the overall observable properties will have a contribution from all the above components [26]. From the measurement results of impedance modulus $|Z|(f)$ and phase $\phi(f)$ frequency

dependent, real and imaginary components $Z'(f)$, $Z''(f)$ have been determined. Fig. 6 shows the frequency variation f of Z' and Z'' on a logarithmic scale. The $Z''(f)$ curves in Fig. 6b show a peak at a characteristic frequency f_{max} showing the relaxation of the carriers (electrons or holes) under the applied AC electric field. Fig. 7 shows the Nyquist - $Z''-Z'$ curves of the samples. In the frequency range of the measurements, the Nyquist curves of the doped samples $0.02 \leq x \leq 0.1$ represent a semi-arc (Fig. 7b) while for the sample $x = 0$, in addition to the semi-arc there is also a secondary increase of $-Z''$ in the increasing direction of Z' corresponds to the low-frequency region. This result and the DC measurement results together show that the Zn doping increases the conductivity in the particles and the semi-arc on the Nyquist curve represents the contribution of the grain boundary resistance. For the pure sample $x = 0$, the observed semi-arc is the contribution of the particle resistance, and the subsequent increase of $-Z''$ with respect to Z' can be explained as the appearance of a semi-arc characteristic for the contribution of the grain boundary that is not observed due to the limitation of the measurement frequency (Fig. 7a).

The Nyquist curves of the samples are fitted based on equivalent circuit models [27]. For the doped samples, the simulation circuit shown in Fig. 8b consists of a resistor R_s connected in series with the system R_1, C_1 in parallel. For the pure sample $x = 0$, the simulation circuit (Fig. 8a) consists of two systems R_1, C_1 , and R_2, C_2 connected in series. The fitting results are shown by solid lines in Fig. 7. The electrical parameters inferred from the fitting process are listed in Table 2. The resistance values are in $M\Omega$ scales, and the capacitance values are in the 10^{-7} F scale. For doped samples, the R_s values obtained are consistent with the resistance values derived from the $I-V$ measurement. These results suggest that the observed DC conduction on the doped samples is caused by the tunneling of the carriers across the highly resistive grain boundary. For the $x = 0$ sample, the large particle resistance corresponds to a very small carrier concentration, so the tunneling process of the carriers cannot be observed through the $I-V$ measurement.

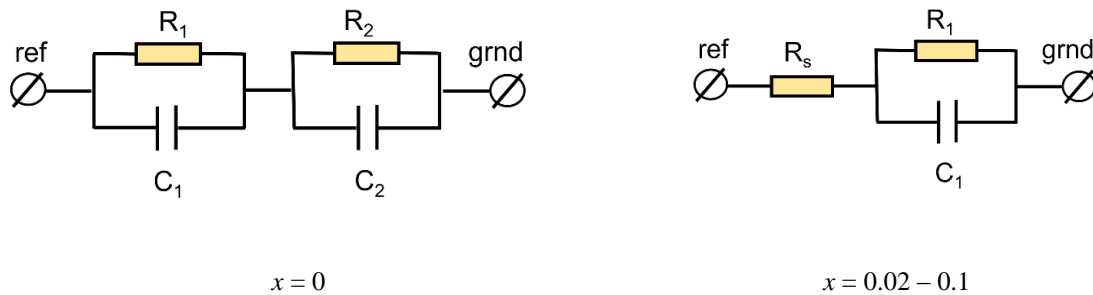


Figure 8. Simulation circuit diagram of series C.

Table 2. The electrical parameters derived from the complex impedance diagram of series C

Samples	$R_s (M\Omega)$	$R_l (M\Omega)$	$C_l (F)$	$R_2 (M\Omega)$	$C_2 (F)$
$x = 0$	-	72.7	7.8×10^{-8}	147.4	1.29×10^{-6}
$x = 0.02$	10.8	42.51	1.08×10^{-7}	-	-
$x = 0.04$	3.7	17.98	2×10^{-7}	-	-
$x = 0.06$	0.7	62.07	5.89×10^{-7}	-	-
$x = 0.08$	0.47	106.83	1.06×10^{-7}	-	-
$x = 0.1$	0.48	65.38	2.5×10^{-7}	-	-

4. Conclusion

Crystalline grain samples of a single-phase of $Y_3Fe_{5-x}Zn_xO_{12}$ ($x = 0 - 0.1$) were successfully fabricated by the sol-gel method combined with annealing at $900\text{ }^\circ\text{C}$ for 5 h, heating rate of $2\text{ }^\circ\text{C}/\text{min}$. The process of investigating the influence of manufacturing conditions shows that the heating rate strongly affects the phase formation of the grain sample. The lattice constant and saturation results indicate that the Zn^{2+} doped ions are in the octahedral sublattice of the crystal structure. The charge imbalance due to the presence of Zn^{2+} ions causes the resistance of the doped samples to decrease by 5-6 orders in magnitude compared with the pure YIG samples prepared by the same method. Analysis of the Nyquist curves at room temperature has shown the influence of grain boundaries on the total impedance of the particles. The results can be well-fitted based on equivalent circuit models. The process of electrical conduction between particles when DC voltage is applied is explained due to the implicit penetration of the carriers through the grain boundary potential barrier.

Acknowledgment

The research is funded by the Hanoi University of Science and Technology (HUST) under project number T2020 – SAHEP – 019.

References

- [1] M. A. Gilleo, *Ferromagnetic Materials: Handbook of Magnetic Materials*, North-Holland Publishing Company, Vol. 2, 1980.
- [2] S. Hosseinzadeh, L. Jamilpanah, J. S. E. Gharehbagh, M. Behboudnia, A. Tiwari, S. M. Mohseni, Effect of YIG Nanoparticle Size and Clustering in Proximity-Induced Magnetism in Graphene/YIG Composite Probed with Magnetoimpedance Sensors: Towards Improved Functionality, Sensitivity and Proximity Detection, *Compos. Part B Eng.*, Vol. 173, 2019, pp. 1-16, <https://doi.org/10.48550/arXiv.1811.12317>.
- [3] H. Li, Y. Guo, Synthesis and Characterization of YIG Nanoparticles by Low Temperature Sintering, *J. Mater. Sci. Mater. Electron.*, Vol. 29, 2018, pp. 9369-9374, <https://doi.org/10.1007/s10854-018-8968-5>.
- [4] P. V. Shinde, C. S. Rout, *Magnetic Gas Sensing: Working Principles and Recent Developments*, *Nanoscale Adv.*, Vol. 3, 2021, pp. 1551-1568, <https://doi.org/10.1039/D0NA00826E>.
- [5] I. Nadinov, O. Kovalenko, J. L. Rehspringer, M. Vomir, L. Mager, Limits of the Magneto-Optical Properties of Bi: YIG Films Prepared on Silica by Metal Organic Decomposition, *Ceram. Int.*, Vol. 45, 2019, pp. 21409-21412, <https://doi.org/10.1016/j.ceramint.2019.07.129>.
- [6] S. M. Elhamali, N. B. Ibrahim, S. Radiman, Structural, Optical and Magnetic Properties of YIG and TbErIG Nanofilms Prepared Using A Sol-gel Method, *Mater. Res. Bull.*, Vol. 112, 2019, pp. 66-76, <https://doi.org/10.1016/j.materresbull.2018.12.005>.
- [7] M. Baziljevich, D. Barness, M. Sinvani, E. Perel, A. Shaulov, Y. Yeshurun, Magneto-Optical System for High Speed Real Time Imaging, *Rev. Sci. Instrum.*, Vol. 83, 2012, <https://doi.org/10.1063/1.4746255>.
- [8] Y. Liu, P. Zhou, R. Bidthanapally, J. Zhang, W. Zhang, M. R. Page, G. Srinivasan, Strain Control of Magnetic Anisotropy in Yttrium Iron Garnet Films in A Composite Structure with Yttrium Aluminum Garnet Substrate, *J. Compos. Sci.*, Vol. 6, 2022, pp. 1-14, <https://doi.org/10.3390/jcs6070203>.
- [9] A. D'Amico, P. D. Gasperis, Semiconducting Properties of A Low Resistive Ca-Doped YIG Film, *J. Appl. Phys.*, Vol. 53, 1982, pp. 8225, <https://doi.org/10.1063/1.330334>.
- [10] A. D. Amico, A. Grilli, A. Paoletti, P. Paroli, A. Tucciarone, Doped Yttrium Iron Garnet for Thermistor Bolometers, *Mat. Res. Bull.*, Vol. 19, 1984, pp. 347-354, [https://doi.org/10.1016/0025-5408\(84\)90177-6](https://doi.org/10.1016/0025-5408(84)90177-6).

- [11] A. D'Amico, P. D. Gasperis, A. Grilli, A. Paoletti, G. Perocco, Calcium Doped Yttrium Iron Garnet Films for Temperature Sensors, *Thin Solid Films*, Vol. 129, 1985, pp. 151-159, [https://doi.org/10.1016/0040-6090\(85\)90103-8](https://doi.org/10.1016/0040-6090(85)90103-8).
- [12] G. H. Jonker, Analysis of the Semiconducting Properties of Cobalt Ferrite, *J. Phys.Chem. Solids*, Vol. 9, 1959, pp. 165-175, [https://doi.org/10.1016/0022-3697\(59\)90206-9](https://doi.org/10.1016/0022-3697(59)90206-9).
- [13] R. Metselaar, M. A. H. Huyberts, Nonstoichiometry and Electronic Defects in Yttrium Iron Garnet, *J. Solid State Chem.*, Vol. 22, 1977, pp. 309-319, [https://doi.org/10.1016/0022-4596\(77\)90007-X](https://doi.org/10.1016/0022-4596(77)90007-X).
- [14] N. P. Duong, D. T. T. Nguyet, T. T. Loan, L. N. Anh, S. Soontaranon, W. Klysubun, T. T. V. Nga, Effects of Sn⁴⁺ Doping and Oxygen Vacancy on Magnetic and Electrical Properties of Yttrium Iron Garnet Prepared by Sol-Gel Method, *Ceram. Int.*, Vol. 47, 2021, pp. 6442-6452, <https://doi.org/10.1016/j.ceramint.2020.10.226>.
- [15] R. P. Garcia, A. Delgado, Y. Guerra, G. Duarte, L. A. P. Gonçalves, E. P. Hernández, The Synthesis of Single-Phase Yttrium Iron Garnet Doped Zinc and Some Structural and Magnetic Properties, *Mater. Res. Express*, Vol. 4, 2017, pp. 0-8, <https://doi.org/10.1088/2053-1591/aa557a>.
- [16] R. P. Garcia, A. Delgado, Y. Guerra, B. V. M. Farias, D. Martinez, E. Skovroinski, A. Galembeck, E. P. Hernandez, Magnetic and Structural Properties of Zn-Doped Yttrium Iron Garnet Nanoparticles, *Phys. Status Solidi Appl. Mater. Sci.*, Vol. 213, 2016, pp. 2485-2491, <https://doi.org/10.1002/pssa.201533078>.
- [17] D. Bokov, A. T. Jalil, S. Chupradit, W. Suksatan, M. J. Ansari, I. H. Shewael, G. H. Valiev, E. Kianfar, Nanomaterial by Sol-Gel Method: Synthesis and Application, *Adv. Mater. Sci. Eng.*, 2021, <https://doi.org/10.1155/2021/5102014>.
- [18] Y. Guo, H. Li, S. Li, L. Chen, Z. Li, Study on the Structure, Magnetic Properties and Mechanism of Zn-Doped Yttrium Iron Garnet Nanomaterial Prepared by the Sol-gel Method, *Gels*, Vol. 8, No. 5, 2022, <https://doi.org/10.3390/gels8050325>.
- [19] R. P. Garcia, Y. Guerra, F. E. P. Santos, L. C. Almeida, E. P. Hernández, Structural and Magnetic Properties of Ni-Doped Yttrium Iron Garnet Nanopowders, *J. Magn. Magn. Mater.*, Vol. 492, 2019, pp. 165650, <http://doi.org/10.1016/j.jmmm.2019.165650>.
- [20] Z. Zhang, K. Singh, Y. Tsur, J. Zhou, J. J. Dynes, V. Thangadurai, Studies on Effect of Ca-doping on Structure and Electrochemical Properties of Garnet-type Y_{3-x}Ca_xFe₃O_{12-Δ}, *J. Solid State Chem.*, Vol. 290, 2020, pp. 121530, <https://doi.org/10.1016/j.jssc.2020.121530>.
- [21] H. S. Aziz, S. Rasheed, R. A. Khan, A. Rahim, J. Nisar, S. M. Shah, F. Iqbal, A. R. Khan, Evaluation of Electrical, Dielectric and Magnetic Characteristics of Al-La Doped Nickel Spinel Ferrites, *RSC Adv.*, Vol. 6, No. 8, 2016, pp. 6589-6597, <https://doi.org/10.1039/C5RA20981A>.
- [22] J. M. Montes, F. G. Cuevas, J. Cintas, Porosity Effect on the Electrical Conductivity of Sintered Powder Compacts, *Appl. Phys. A Mater. Sci. Process.*, Vol. 92, No. 2, 2008, pp. 375-380, <https://doi.org/10.1007/s00339-008-4534-y>.
- [23] A. A. Akl, Optical Properties of Crystalline and Non-crystalline Iron Oxide Thin Films Deposited by Spray Pyrolysis, *Appl. Surf. Sci.*, Vol. 221, 2004, pp. 319-329, <https://doi.org/10.1016/j.apsusc.2004.03.263>.
- [24] M. Guziewicz, J. Grochowski, M. A. Borysiewicz, E. Kaminska, J. Z. Domagala, W. Rzdokiewicz, B. S. Witkowski, K. Golaszewska, R. Kruszka, M. Ekielski, A. Piotrowska, Electrical and Optical Properties of NiO Films Deposited by Magnetron Sputtering, *Optica Applicata XLI*, Vol. 2, 2011, pp. 431-440, <https://doi.org/10.1016/j.surfcoat.2004.10.032>.
- [25] W. T. Li, D. R. McKenzie, W. D. McFall, Q. C. Zhang, W. Wiszniewski, Breakdown Mechanism of Al₂O₃ Based Metal-to-Metal Antifuses, *Solid State Electron*, Vol. 44, 2000, pp. 1557-1562, [https://doi.org/10.1016/S0038-1101\(00\)00125-8](https://doi.org/10.1016/S0038-1101(00)00125-8).
- [26] A. J. Moulson, J. M. Herbert, *Electroceramics: Materials, Properties, Applications*, John Wiley & Sons, Ltd, 2003, pp. 569.
- [27] P. Chaitanya, A. Shukla, L. Pandey, Determination of Equivalent Circuit Model Components of Piezoelectric Materials by using Impedance Spectroscopy, *Integr. Ferroelectr.*, Vol. 150, No. 1, 2014, pp. 88-95, <https://doi.org/10.1080/10584587.2014.874274>.